Journal of Manufacturing Processes 80 (2022) 765–774

Contents lists available at ScienceDirect

Journal of Manufacturing Processes

journal homepage: www.elsevier.com/locate/manpro

Development of a phased array ultrasound roller probe for inspection of wire + arc additive manufactured components

Randika K.W. Vithanage [a,*], Ehsan Mohseni [a], David Lines [a], Charalampos Loukas [a], Euan Foster [a], Charles N. MacLeod [a], S. Gareth Pierce [a], Anthony Gachagan [a], Jialuo Ding [b], Stewart Williams [b]

[a] Department of Electronic & Electrical Engineering University of Strathclyde, United Kingdom
[b] Welding Engineering & Laser Processing Centre, University of Cranfield, United Kingdom

ARTICLE INFO

Keywords:
Phased array ultrasound imaging
Wire + arc additive manufacturing
In-process phased array inspection
Non-destructive testing of additive manufacturing
Ultrasound phased array roller probe

ABSTRACT

The wire + arc additive manufacturing (WAAM) process, which combines an electric arc as a heat source and metal wire as feedstock is proving to be very effective when producing medium to large scale metal components. The non-destructive testing (NDT) of WAAM parts, while they are being produced, provides early intervention opportunities to rectify manufacturing nonconformities and to perform in-process quality assurance of the parts. This attracts a significant amount of material, time and cost savings. Therefore, this paper presents the research, development and validation of a high temperature phased array ultrasound testing (PAUT) roller probe to perform robotically delivered in-process NDT of WAAM components. The experimental results confirm that the PAUT roller probe can endure surface temperatures up to 350 °C, can be autonomously deployed via a robotic arm and can detect 1 mm diameter flat-bottom holes located 6 mm, 9 mm and 12 mm deep under the unmachined surface of a Ti-6Al-4V WAAM calibration block.

1. Introduction

Additive manufacturing (AM) is a promising alternative to conventional subtractive manufacturing, especially when producing high-value metal components with complex geometries [1]. Some of the key advantages of AM include shorter lead times, improved buy-to-fly ratios, reduced number of assembly components, ability to produce low volume – high mix components and improved manufacturability of parts with intricate geometries [2–5]. Among various AM methods, wire + arc additive manufacturing (WAAM) demonstrates the potential in producing large engineering structures with higher deposition rates at a lower cost [6,7]. The core technology of WAAM is based on wire-direct energy deposition (DED) and exploits welding capabilities to combine an electric arc as the heat source and wire as the feedstock to produce near-net-shaped metallic components through layer-wise deposition of materials [7,8].

1.1. Inspection of WAAM using ultrasound

The current research focus of WAAM is on producing large scale functional components in the aerospace, defence, automotive, nuclear and rapid tooling industry [9–11]. Therefore, it is vital to assure the quality and structural integrity of these safety-critical parts. This can be realised through well-established non-destructive testing (NDT) procedures similar to ultrasound testing (UT) [12]. Compared to other NDT techniques such as radiography and eddy current testing, UT and acoustic-based monitoring are non-hazardous and bulk inspection techniques and have a better capability of detecting different types of defects [13–15]. Furthermore, UT inspection has gained a recent reputation with the emergence of phased array ultrasound testing (PAUT) [16]. PAUT provides the ability to focus the UT beam at an intended location providing a better signal to noise ratio (SNR) and the capability to electronically steer the beam, allowing a better surface coverage and a reduced number of raster scan paths [17].

Javadi et al. successfully used a 5 MHz-64 elements PAUT transducer to detect intentionally embedded defects using tungsten carbide balls within mild steel WAAM walls and to detect artificially induced hydrogen cracks within welded components [18,19]. Both the radiographic testing and the ultrasonic testing of WAAM parts were evaluated by [20] and concluded that both techniques could potentially be used to

* Corresponding author.
E-mail address: randika.vithanage@strath.ac.uk (R.K.W. Vithanage).

https://doi.org/10.1016/j.jmapro.2022.06.045
Received 15 February 2022; Received in revised form 19 May 2022; Accepted 17 June 2022
Available online 25 June 2022
1526-6125/© 2022 The Authors. Published by Elsevier Ltd on behalf of The Society of Manufacturing Engineers. This is an open access article under the CC BY license (http://creativecommons.org/licenses/by/4.0/).

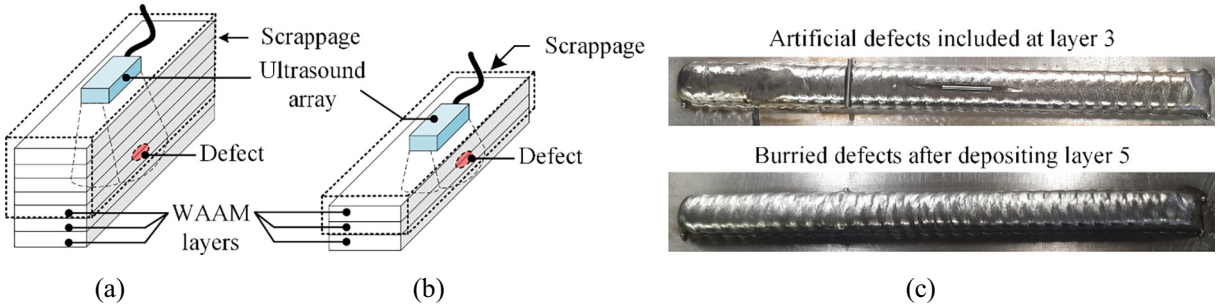


Fig. 1. UT inspection and scrappage due to (a) post-process inspection, (b) in-process inspection of WAAM components and (c) example WAAM component with intentional defects embedded at layer three and fully covered after depositing layer five.

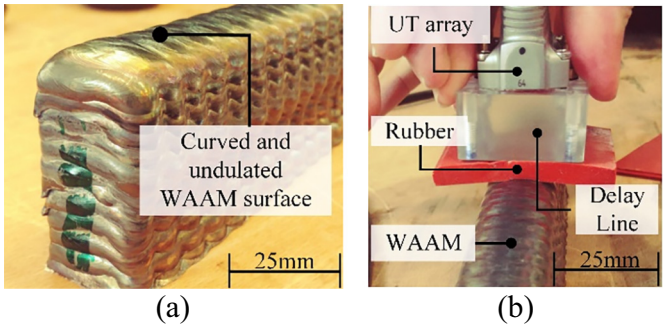


Fig. 2. (a) Laterally curved and the undulated surface of a straight WAAM wall and (b) rubber as a geometrically compliant interface.

inspect WAAM samples. The suitability of PAUT in WAAM inspection is further analysed by [21]. Here, the authors concluded that PAUT technology could be used to detect defects within WAAM walls and determine their size, morphology, and location. The applicability of PAUT in the inspection of aluminium WAAM components was further assessed by [22]. It was claimed that PAUT could detect defects with varying sizes between 0.6 mm to 1 mm.

1.2. In-process inspection of WAAM

As WAAM builds the 3D shape of a part by depositing subsequent material layers on the previous layers, defects such as lack of fusion, porosity, keyholes, cracks and inclusion may have occurred at an early stage of deposition, are now buried within the WAAM part. Traditionally, these defects are undetected until post-process inspection is performed [23]. This leads to expensive, complicated and time-consuming rework, longer product cycle times, and diminished throughput [24].

Therefore, merging the WAAM deposition and the inspection into a single process - termed in-process inspection or in-process screening of WAAM is desirable. This provides the capability to identify and remove/repair flaws while the material is being deposited and the opportunity for early intervention to fine-tune process parameters before subsequent layers are deposited. Hence, this offers the potential to significantly reduce material wastage, rework costs, downtime and improve lead-time. Illustrated in Fig. 1(a) and (b) are the post-process inspection and in-process inspection of a WAAM wall using an ultrasound probe and a defect buried at an early-stage deposition. Fig. 1(c) shows a representative WAAM wall with buried intentional defects (embedded at layer three) after depositing five layers.

1.3. Challenges with in-process inspection

The objective of this body of work was to research, design and develop a PAUT probe for in-process inspection of WAAM parts. The

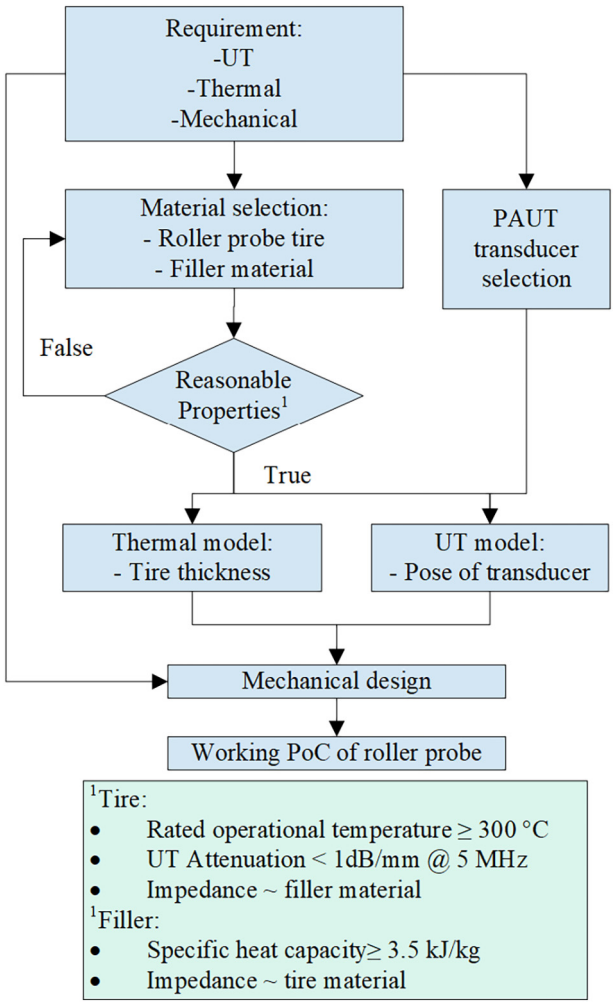


Fig. 3. Generic workflow of the roller probe development with ideal properties.

typical WAAM deposition environment is relatively hostile, from an NDT perspective, when considering temperatures, coupling and electromagnetic interference, which drives a requirement for automation of deployment. Some of the main challenges associated with implementing in-process ultrasound inspection of WAAM components include high temperatures, the complex surface profile and roughness of WAAM parts, electrical isolation between the transducer–workpiece interface and various other specifications vital for automation such as the ability for easy manipulation of the probe on a given workpiece with minimal hardware deterioration. The undulated nature and lateral curvature of an unmachined straight WAAM wall are shown in Fig. 2(a).

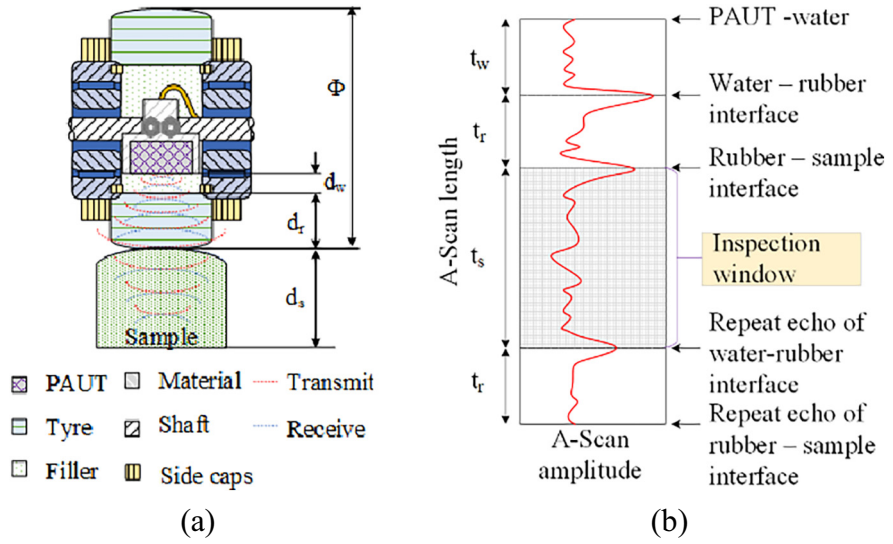


Fig. 4. (a) Schematic of the roller probe illustrating array configuration, positioning on a WAAM sample and indicative transmit-receive ultrasound wave and (b) A-Scan signal illustrating surface echoes.

To satisfy such demands, an autonomous deployable roller probe designed to inspect WAAM components in-process is introduced. This PAUT roller probe is configured to perform linear or sectorial scans creating longitudinal waves into the material. The roller probe tyre enables conformance to the undulating and curved WAAM surfaces. The effect of having an intermediate rubber layer that conforms to WAAM curvatures is shown in Fig. 2(b) using a 0° wedge assembly and a 6 mm thick silicone rubber layer. The roller probe introduced here can either be configured to travel behind a WAAM deposition head at a pre-determined distance as each WAAM layer is deposited or perform discrete layer scans at a higher travel speed after deposition of single/multiple WAAM layer/s.

The overall design and development of the PAUT roller probe were progressed from fundamental modelling to a detailed design of a working prototype. Multiple iterations and intermediate validations were performed to improve the thermal and ultrasound characteristics. Finally, a proof of concept (PoC) of the PAUT roller probe was assembled and validated using a Ti-6Al-4V WAAM calibration block. This manuscript is structured as follows: Section 2 describes the modelling, design and development of the PAUT roller probe, Section 3 presents experimental setups and discusses critical results, and Section 4 concludes the current work and summarises the future work.

2. Design and development

The overall roller probe development workflow is presented in Fig. 3. In the first stage, the technical requirement and challenges associated with deploying a robotically delivered contact ultrasonic probe for in-process WAAM inspection were analysed.

Here, the overall design strategy was governed by several factors such as (i) requirement to operate at high temperatures, (ii) inspection through as-built (unmachined) WAAM surfaces, (iii) acoustic properties of coupling materials and their malleability, (iv) ultrasound transducer size, (v) internal pressure of the roller probe's liquid domain, (vi) transducer cable routing limitations, (vii) capability to be deployed by robotic manipulators and (viii) necessary ingress protection (IP) rating levels.

It was assumed that the tyre acts as the primary thermal barrier of the roller probe. A thicker tyre provides better thermal insulation but further attenuates the acoustic wave energy. Therefore, the roller probe's tyre thickness was optimised to withstand 350 °C WAAM surface temperature for at least 10 min. This temperature simulates the maximum operating temperature of the rubber and also accommodates common WAAM interpass temperatures [25]. The simulation setup was similar to the methodology reported in [26].

Table 1
Key components and their material properties: sound velocity (m s^{-1}) and density (kg m^{-3}) at 25 °C.

Component	Material	Sound velocity	Density
Filler	Water	1480	1000
Tyre	Silicone rubber	1000	1020
Sample	Ti	6100	4430
	Al	6300	2840
	Steel	5920	7850
	Inconel	5700	8193

2.1. The conceptualisation of roller probe for WAAM inspection

The configuration and working principle of a PAUT roller probe is illustrated in Fig. 4(a) using a cross-sectional view where the positioning of the roller probe on a WAAM sample, different material domains and indicative transmit-receive ultrasound waves are shown. The UT array is assumed to be placed horizontally within an enclosed liquid domain to undertake 0° inspection, where the ultrasound wave travels through the fluid domain and silicone rubber tyre before reaching the WAAM material. Strong interface reflection echoes may occur when the UT signal travels through different materials due to poor coupling and/or mismatches in acoustic impedance [27].

As the ultrasonic wave reflects from the varying interfaces, the wave echoes will appear with a gradually reduced amplitude, due to attenuation, throughout the full A-Scan length – see Fig. 4(b), where multiple material interfaces are marked on an illustrative A-Scan signal. Since there is a possibility that these repeat echoes mask the useful field of a scanned image, it is required to determine the appropriate thickness and wave velocity of each material such that the repeat echoes do not disrupt the desired inspection window.

As shown in Fig. 4(a), the primary axis of the UT array was oriented along the transversal (Y) axis of the WAAM sample to maximise the UT inspection coverage of the WAAM width for a given scan path. Published work in [26] highlighted the promising use of silicone rubbers which are acoustically optimised and able to withstand temperatures up to 350 °C. Due to the non-planar surface profile of the as-built WAAM surface, softer conformable silicone rubbers were developed and deployed to

Table 2
Minimum water path required to have at least 20 mm deep scan window in different WAAM materials.

WAAM material	Minimum d_w (mm)
Ti	13.72
Al	13.57
Mild steel	13.87
Inconel	14.06

Table 3
Wavelength and near field of roller probe assembly for different materials at 5 MHz PAUT transducer frequency.

WAAM material	Sensitivity (mm)				Near field N_{rp} (mm)
	10 MHz	7.50 MHz	5 MHz	2.50 MHz	
Ti	0.31	0.41	0.61	1.22	48.95
Al	0.32	0.42	0.63	1.26	45.22
Mild steel	0.30	0.39	0.59	1.18	49.70
Inconel	0.29	0.38	0.57	1.14	48.31

fully wrap across the WAAM component's upper surface and remove any entrapped pockets of air. The optimised rubber features a longitudinal attenuation of 0.90 dB/mm at 5 MHz. The roller probe is filled with water owing to its specific heat capacity (4182 J/kg °C) and low acoustic impedance mismatch (<0.38 MRayls) with the silicone rubber tyre. By assuming the height of a given WAAM layer ≤ 2.0 mm [28], the roller probe was designed to have a 20.0 mm acoustic window to accommodate at least ten WAAM layers made of materials such as titanium, aluminium, and mild-steel and Inconel alloys [7]. Relevant acoustic and mechanical properties of these materials that have been considered in this study are listed in Table 1.

2.2. Ultrasound modelling and simulations

2.2.1. Water path height calculation

The length of the scan window was estimated to be $d_s \geq 20.0$ mm to inspect at least 10 WAAM layers manufactured with the current deposition strategy, and the roller probe's tyre thickness was considered to be $d_r = 6.0$ mm based on thermal simulations. It is required to determine a water path height d_w such that the repeat echo of the water-probe tyre interface does not mask the user-defined scan window. The relationship expressed in Eq. (1) was realised by observing the A-Scan length in the time domain from the ultrasonic transducer to the first repeat echo of the water-tyre interface. Here, t_w, t_r and t_s are the total time that the ultrasonic signal travelled through the water domain, tyre and sample, respectively. As indicated in Eq. (2), an analytical solution for d_w can be realised by assuming the longitudinal acoustic wave velocity within water V_w, probe tyre material V_r and sample V_s.

$$2 \times t_w \geq t_w + t_r + t_s \tag{1}$$

$$d_w \geq V_w \times \left(\frac{d_r}{V_r} + \frac{d_s}{V_s}\right) \tag{2}$$

The minimum water path height required within the roller probe for different WAAM materials is summarised in Table 2. The commercial phased array transducer housing used in this development has a 20.0 mm height making the water path $d_w = 29.0$ mm for a 6.0 mm thick tyre. Based on the thermal and acoustic models, this water path depth is thermally safer to have a 10 min initial scan time and acoustically capable of having a 20.0 mm deep scan window into a given WAAM material.

2.2.2. Transducer frequency and nearfield analysis

A minimum defect size of 1.0 mm, was deemed a target aim of the in-process WAAM screening application. The sensitivity of the ultrasound transducer is given by the half-wavelength of the acoustic wave within a given material and increases with the central frequency of the array [29]. The wavelength λ of an acoustic signal inside a WAAM section is given according to Eq. (3) where f is the central frequency of the array. The detection sensitivities within each WAAM material were calculated for a range of frequencies commonly deployed in NDE, with centre frequencies ranging from 2.50 MHz to 10 MHz – see Table 3.

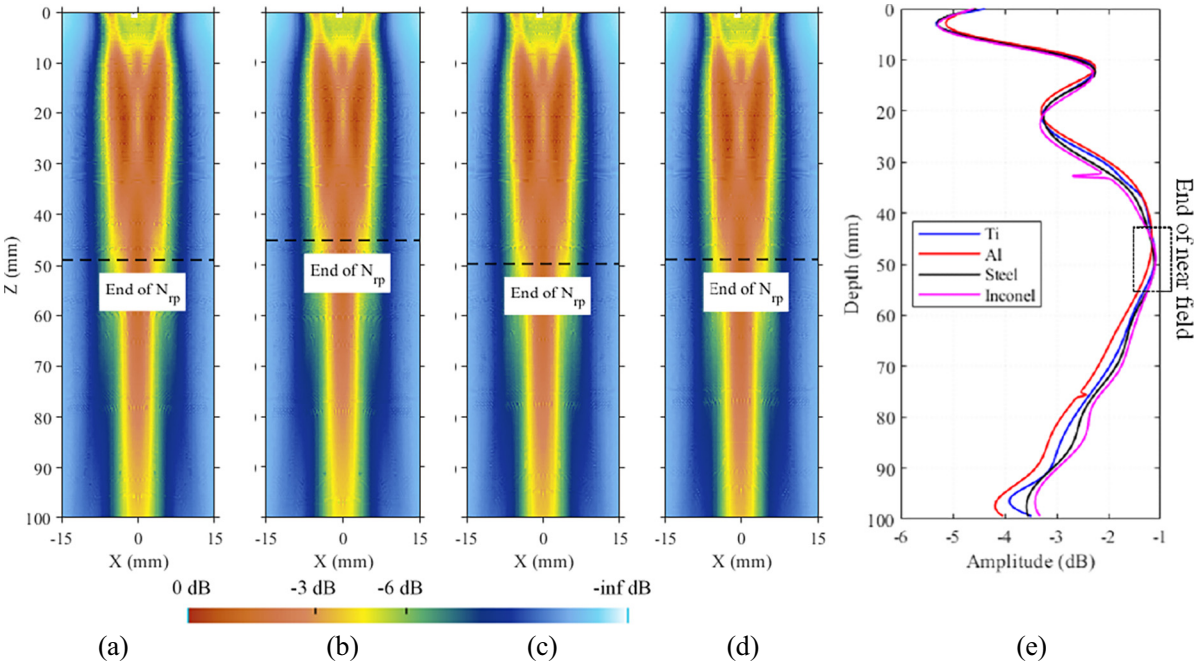


Fig. 5. (a)–(d) Acoustic energy map and end of near field within Ti, Al, Mild steel and Inconel and (e) UT wave energy fluctuation within each material in dB and region end of near filed.

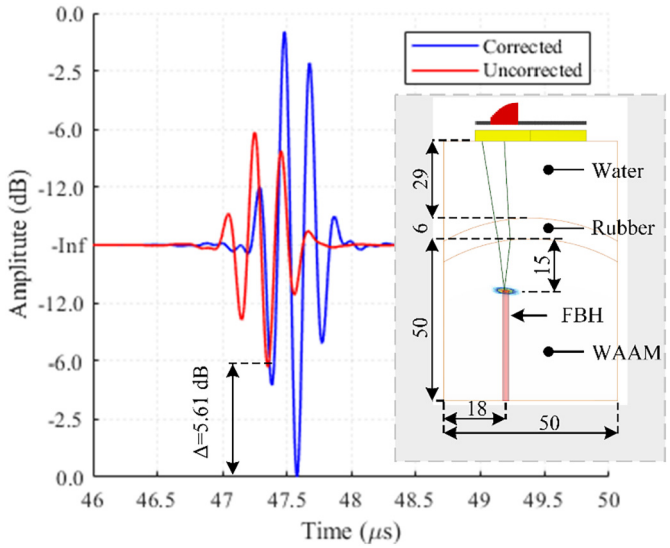


Fig. 6. Illustration of the ultrasound setup mimicking PAUT roller probe and maximum A-Scan signals correspond to FBH with corrected and uncorrected focal laws for the curvature of the simulated WAAM surface.

$$\lambda = \frac{V_w}{f} \tag{3}$$

As acoustic wave attenuation tends to increase with the frequency, it is desirable to select the lowest ultrasound frequency that also meets the required sensitivity [30]. Therefore, given the in-process screening requirement of 1.0 mm, a 5 MHz – 64 elements linear array was found to be the lowest frequency that provides adequate sensitivity within a given WAAM material.

As the acoustic wave propagates through multiple materials before reaching the WAAM sample, it is important to modify focal laws accordingly to have the focus at the intended depth of inspection. This encourages the maximum amount of acoustic energy transmitted into the WAAM material concentrated at a user-defined focal depth. Therefore, it is important for the scan window d_s considered in Section 2.2.1 to be within the nearfield of the UT array where the UT beam focus is possible. The near field is defined as the region in front of a given transducer where the ultrasound energy changes nonuniformly until it reaches a maximum, after which the energy declines gradually [31]. Therefore, a semi-analytical simulation was carried out to determine the near field of the PAUT roller probe (N_{rp}). A 5 MHz 64 element linear commercial phased array with 0.5 mm pitch and 10.0 mm elevation was incorporated into the model. As estimated in Section 2.2.1, a 29.0 mm high water path was introduced to simulate the roller probe's liquid domain and a 6 mm thick rubber layer to simulate the roller probe tyre. A 100 mm high test material was used with parameterised properties to mimic Ti, Al, Mild steel and Inconel. A sub-aperture of 32 elements was selected to provide a balance between the transversal WAAM wall coverage and the resultant SNR of any defects within the inspection window.

Fig. 5(a)–(d) shows the UT energy intensity map within Ti, Al, Mild steel and Inconel test samples. The graph shown in Fig. 5(e) indicates the maximum ultrasound wave amplitude that marks the end of the near field within individual material. The N_{rp} value for each material is summarised in Table 3 and it can be observed that approximately $N_{rp} \geq$ 45 mm, comparatively within the expected inspection window of the PAUT roller probe.

2.2.3. Effect of WAAM curvature on beamforming

Due largely to the current deposition technology and dynamics of the material melt pool, a noticeable lateral curvature is observed on deposited WAAM layers. This phenomenon requires deformation of the PAUT roller probe tyre to enable conformance of the acoustic tyre to the complex surface, as indicated in Fig. 2(a). Therefore, it is important to consider the lateral WAAM curvature when generating PAUT focal (delay) laws. A semi-analytical simulation was performed to validate the effect of correctly formed beams that offset the WAAM surface curvature.

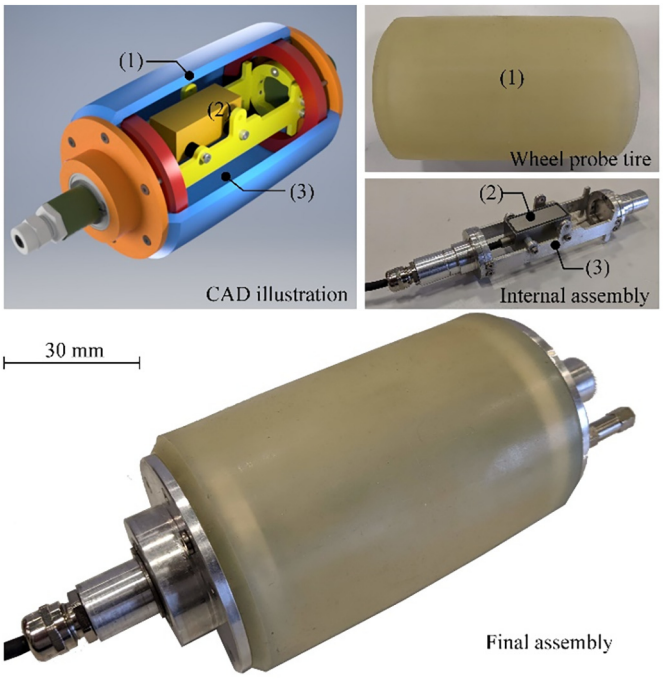


Fig. 7. Computer-aided design and physical assembly of the PAUT roller probe: (1) silicone tyre, (2) 5 MHz-64 element linear PAUT and (3) PAUT carrier.

The inspection setup illustrated in Fig. 6 was assumed to simulate the roller probe placed on a WAAM surface. A 5 MHz – 64 element linear array was used on a 50 mm wide WAAM sample with a 60 mm radius of surface curvature. The physical dimensions of the roller probe were simulated with a 29.0 mm high water path and a 6 mm thick silicone rubber tyre. A 1.0 mm diameter Flat Bottom Hole (FBH) was placed 15.0 mm deep and 7.0 mm off the centre of the sample. It was assumed that the roller probe's tyre conforms to and follows the lateral curvature of the WAAM sample.

Two phased array linear sweeps focused 15 mm deep in the sample, where one assuming the surface is flat (uncorrected) and another taking the WAAM surface curvature into account (corrected), were generated and included in the model. The amplitudes of both A-Scan signals were converted to decibels concerning the maximum amplitude provided by the corrected A-Scan. As shown in Fig. 6, a significant amplitude drop of 5.60 dB was observed when the beam was not focused (curved surface correction was not taken into account) as compared to when accounting for the WAAM surface curvature. Therefore, it is evident that compensation for the WAAM surface curvature is important for achieving an effective beam focus within the material and an obtaining acceptable SNR.

2.3. Mechanical design and assembly

A mechanical model of the PAUT roller probe was developed using a Computer-Aided Design (CAD) package. The individual component was parameterised and linked at a part level to improve the reconfigurability and flexibility of the final CAD assembly. The critical mechanical, thermal and ultrasound aspects which were numerically determined and experimentally validated were incorporated into this mechanical model. All bearings, hydraulic seals and cable glands used in the roller probe are

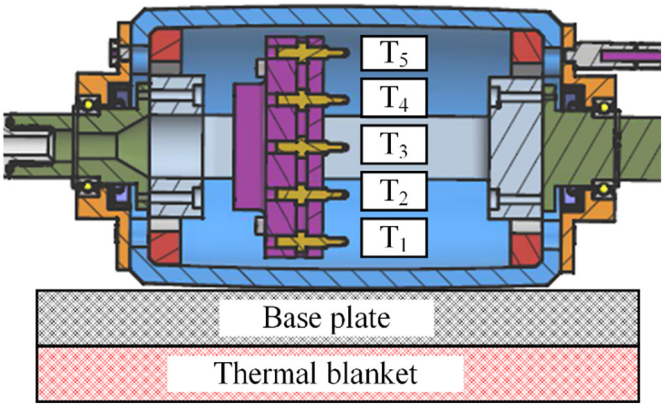


Fig. 8. Cross-sectioned roller probe assembly illustrating thermistor carriage with internal assembly structure within the roller probe and thermal blanket arrangement.

rated at IP 67. A mechanical PoC of the roller probe was assembled using a 3D printed tyre from a rubber-like material and tested for 1.25 bar hydraulic pressure. Illustrated in Fig. 7 is the CAD of the roller probe, silicone rubber tyre, physical carrier assemblies and final assembly of the roller probe.

3. Experimental setup and results

3.1. Thermal experiments and results

The internal temperature distribution of the roller probe was experimentally examined in a similar process as Section III.A in [26]. Here, a pseudo roller probe containing an array of thermistors (Ti: $i = 1, \ldots, 5$) as illustrated in Fig. 8, National Instrument data acquisition hardware and LabVIEW software were used to record the probe's liquid domain temperature. The roller probe was robotically deployed onto a heated steel plate and programmatically manipulated across the plate until any thermistor exceeded a threshold of 50 °C simulating the rated operational temperature of the ultrasound array.

The initial scan time of the roller probe before exceeding the liquid domain temperature of 50 °C versus metal baseplate temperature is summarised in Fig. 9(a). A clear temperature gradient across the roller

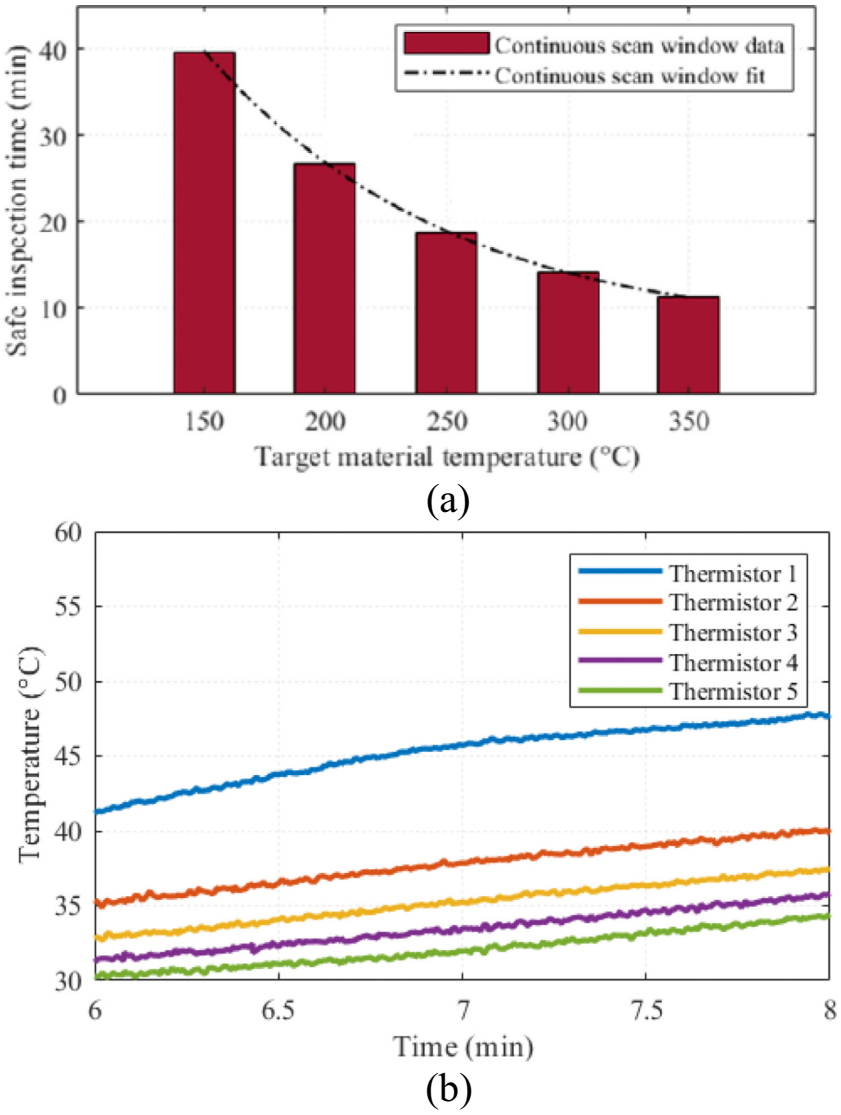


Fig. 9. (a) Continuous scan window of the liquid-filled roller probe for different base plate temperatures and (b) internal temperature distribution within the liquid domain.

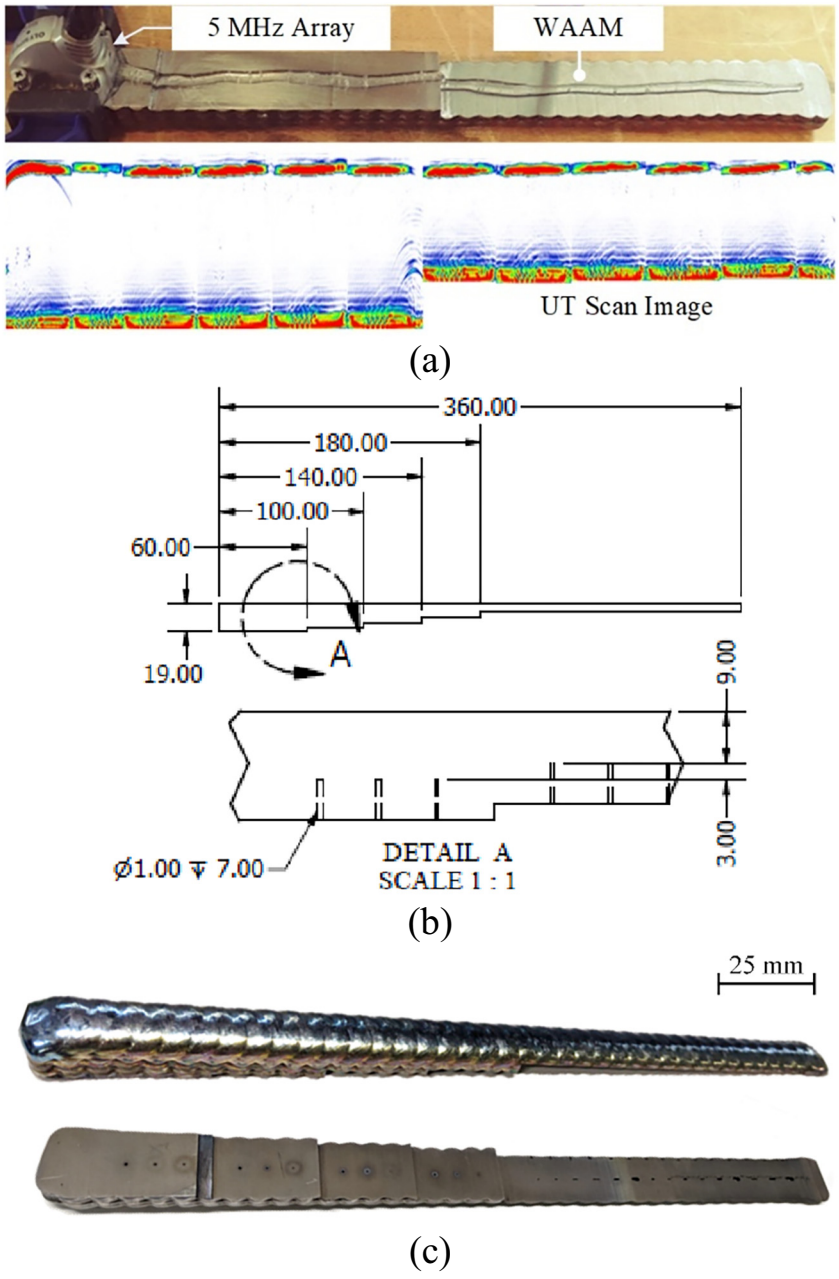


Fig. 10. WAAM calibration block. (a) Initial screening method and UT scan image of the extracted WAAM sample, (b) calibration block dimensions and (c) top and bottom view of the 26 mm wide WAAM calibration block.

probe's liquid domain height was observed throughout all experiments. This indicates that no significant mechanical mixing takes place at lower probe velocities. For example, Fig. 9(b) illustrates the internal temperature distribution of the roller probe, after being 6 min in contact with the base plate, for 2 min when the base plate was at 200 °C. A similar pattern was observed for all base plate temperatures throughout the experiment.

3.2. WAAM inspection

3.2.1. Calibration block preparation

The performance of the PAUT roller probe was evaluated using a custom-designed and manufactured WAAM calibration block with an unmachined surface. The calibration block was extracted from a Ti-6Al-4V WAAM straight wall component using water jet cutting.

Before further processing, a reference contact inspection was performed on the extracted WAAM section to detect the presence of any defects. Here, a 64 element 5 MHz linear UT array was used. A 1.0 mm flat bottom calibration hole (governed by the accessible machining capabilities) was introduced on a separate but compositionally comparable Ti-6Al-4V WAAM sample at a 40.0 mm depth. The calibration gain was set at 49 dB using the said FBH such that the maximum signal amplitude of the FBH reached 100 % of the screen height. A further +6 dB hardware gain was introduced to double the signal amplitude to have increased sensitivity to point defects smaller than the calibration. The probe was coupled directly onto the machined surface of the extracted block using liquid couplant. Fig. 10(a) shows the inspection arrangement and the linear B-Scan image of the extracted section highlights no undesirable indications.

As indicated in Fig. 10(b), the overall calibration block was designed with multiple reference features that can be used to evaluate various aspects of ultrasound inspection. However, only the FBHs with a 1.0 mm

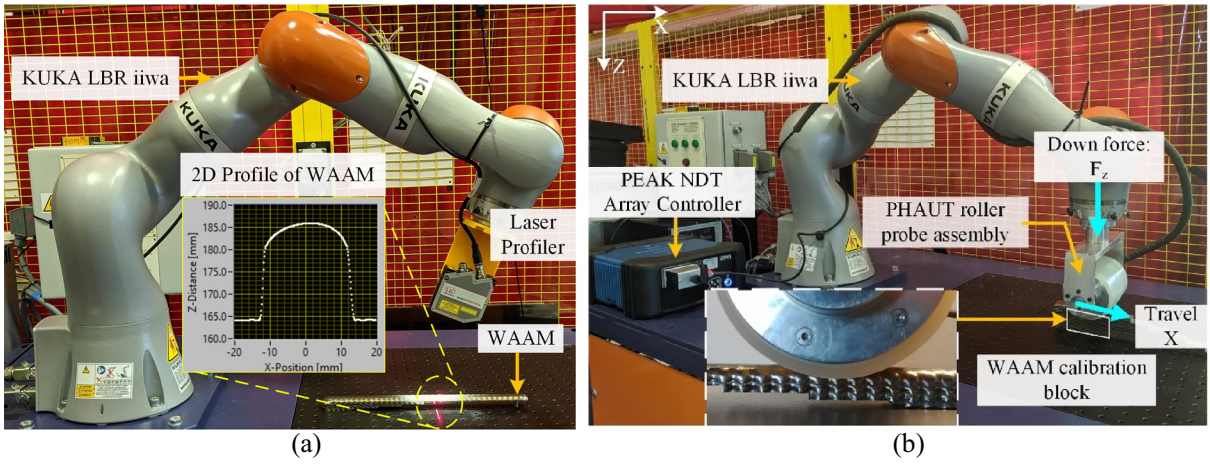


Fig. 11. (a) Quantification of WAAM lateral curvature using a 2D laser profiler and (b) experimental setup illustrating PAUT roller probe, array controller, Ti64 WAAM calibration block with 1 mm FBH and industrial robot with inbuilt force-torque control capability.

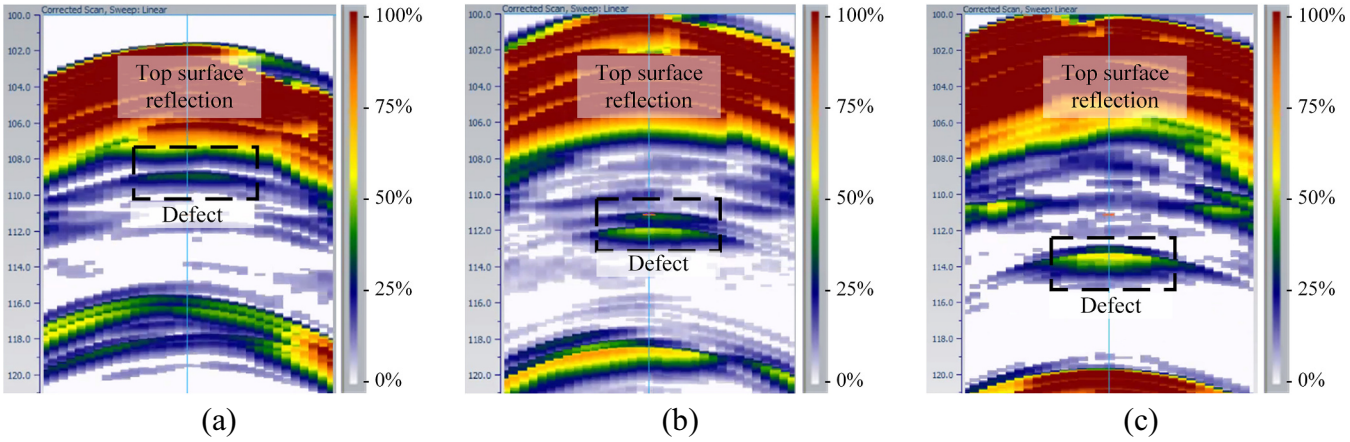


Fig. 12. BScan images of 1 mm Diameter FBHs located at (a) 6 mm, (b) 9 mm and (c) 12 mm depths.

diameter indicated in the figure were used in this research. These features were introduced using the electrical discharge machining (EDM) process. Fig. 10(c) shows the final appearance of the calibration block.

3.2.2. *Corrected focal law generation*

As shown in Fig. 11(a), the lateral curvature of the WAAM calibration block was measured using a 2D laser profiler and it was accounted for in the focal law calculation algorithm to generate a 0° linear scan with 32 sub-aperture. Since a straight WAAM wall was used, it was assumed that the lateral curvature of the sample is approximately similar and unchanged along the length. Here, three separate focal laws with the UT beam focused at 6.0 mm, 9.0 mm and 12.0 mm depths were generated. An LTPA phased array controller (by Peak NDT Ltd., UK) was used to acquire the UT data while an excitation voltage of 100 V, pulse repetition frequency of 2 kHz and hardware gain of 55 dB was selected.

3.2.3. *PAUT roller probe deployment*

Fig. 11(b) shows the roller probe mounted onto a KUKA LBR robot with inbuilt force-torque control/measurement capabilities. This arrangement allowed to manipulate the roller probe over the unmachined WAAM surface along the X-axis (WAAM length) while maintaining the required contact using a 20 N controlled force in the Z direction and normal roller probe orientation to the unmachined WAAM surface. The robot was controlled using an external computer, and the roller probe was acoustically coupled to the as-built WAAM surface using a very thin film of liquid couplant. The ultrasound signal from 1 mm diameter FBHs located at different depths was recorded.

3.3. *Performance of PAUT roller probe*

All three defects simulated using 1.0 mm diameter FBHs were successfully detected through the unmachined WAAM surface using the PAUT roller probe. Fig. 12(a) shows the B-Scan image of the defect located 6 mm deep under the unmachined WAAM surface. Here, the ultrasound signal amplitude was 46 % compared to the calibration reference signal amplitude. Fig. 12(b) and (c) shows the B-Scan images of the remaining FBHs located at 9.0 mm and 12.0 mm depths, respectively. The ultrasound signal from the FBH located 9.0 mm deep was 69 %, while the UT signal from FBH located 12.0 mm deep was 77 % compared to the calibration reference signal amplitude.

As can be seen in all B-Scan images, there is a strong echo from the roller probe tyre and unmachined WAAM surface interface. This is caused by the impedance mismatch between the rubber tyre and the top WAAM surface. Also, it is visible that the ultrasound signal from individual defects improves as the depth from the top WAAM surface to the defect increases. This phenomenon can be explained by the graph shown in Fig. 5(e) – which illustrates ultrasound beam energy within a near field. As it can be seen, the ultrasound beam energy increases with the depth until the end of the near field, providing lower signal amplitude from defects located nearer to the surface and higher signal amplitude

Table 4
UT signal amplitude of individual defect compared to the calibration signal.

Defect nature & diameter	Defect location from the surface	Signal amplitude w.r.t. calibration
FBH: 1.0 mm	6.0 mm	−6.74 dB
FBH: 1.0 mm	9.0 mm	−3.22 dB
FBH: 1.0 mm	12.0 mm	−2.27 dB

from defects located further within the near field. The nature of defects, their location and the obtained ultrasound signal amplitude with reference to the calibration signal are summarised in Table 4.

4. Conclusion

This paper has introduced the design, development and validation of a novel high-temperature PAUT roller probe to perform robotically delivered inspection of WAAM components. The roller probe described here addresses key challenges associated with in-process inspection of WAAM parts, including (i) high temperatures, (ii) inspection through unmachined WAAM surfaces, (iii) continuous inspection with minimal hardware deterioration, (iv) automation capabilities using off-the-shelf robotic manipulators or custom-made gantry systems, and (v) ability to conform to complex WAAM geometries and undulated surfaces.

The experimental results demonstrate that the roller probe can detect artificial point defects simulated by FBHs as small as 1.0 mm in diameter through the unmachined WAAM surface. This roller probe can tolerate temperatures up to 350 °C compared to commercially available roller probes typically limited to 50 °C–60 °C. To summarise, the PAUT roller probe described in this paper has demonstrated:

1. Tolerance to substrate surface temperatures up to 350 °C for more than a 10 min scan window.
2. Ability to perform PAUT inspection on WAAM components while providing an acoustic window deeper than 20 mm within the material to inspect the last 10 WAAM layers assuming the height of a given WAAM layer $\leq$ 2 mm.
3. Promising inspection results with distinctive indications for FBHs of 1.0 mm in diameter at depths of 6.0, 9.0, and 12.0 mm of a Ti-6Al-4V WAAM sample with minimum artefacts obstructing them. The poorest signal associated with the shallowest FBH was only 6 dB lower than the calibration signal.
4. To be fit for in-process or post-process inspection or screening of WAAM components.

Future work seeks to investigate the deployment of this PAUT roller probe within a WAAM deposition cell and evaluate its real-time in-process inspection capabilities using both artificial and real defects. Further activities will investigate the effect of the thermal gradients within the WAAM component and roller probe along with suitable image compensation strategies. Optimised array parameters and frequencies will also be investigated for complex and challenging geometry and WAAM material inspection.

Declaration of competing interest

The authors declare that they have no known competing financial interests or personal relationships that could have appeared to influence the work reported in this paper.

Acknowledgement

This project was funded and supported by New Wire Additive Manufacturing project under EPSRC grant number EP/R027218/1 and the Robotic Wire + Arc Additive Manufacture project under EPSRC grant number EP/P031064/1.

References

[1] Duarte VR, Rodrigues TA, Schell N, Miranda R, Oliveira J, Santos TG. Hot forging wire and arc additive manufacturing (HF-WAAM). Addit Manuf 2020;101193.
[2] Jia C, Liu W, Chen M, Guo M, Wu S, Wu C. Investigation on arc plasma, droplet, and molten pool behaviours in compulsively constricted WAAM. Addit Manuf 2020;101235.
[3] Ke W, Oliveira J, Cong B, Ao S, Qi Z, Peng B, Zeng Z. Multi-layer deposition mechanism in ultra high-frequency pulsed wire arc additive manufacturing (WAAM) of NiTi shape memory alloys. Addit Manuf 2022;50:102513.
[4] Lin Z, Song K, Yu X. A review on wire and arc additive manufacturing of titanium alloy. J Manuf Process 2021;70:24–45.
[5] Rodrigues TA, Bairrão N, Farias FWC, Shamsolhodaei A, Shen J, Zhou N, Maawad E, Schell N, Santos TG, Oliveira JP. Steel-copper functionally graded material produced by twin-wire and arc additive manufacturing (T-WAAM). Mater Des 2022;213:110270.
[6] Artaza T, Suárez A, Veiga F, Braceras I, Tabernero I, Larrañaga O, Lamikiz A. Wire arc additive manufacturing Ti6Al4V aeronautical parts using plasma arc welding: analysis of heat-treatment processes in different atmospheres. J Mater Res Technol 2020;9:15454–66.
[7] Williams SW, Martina F, Addison AC, Ding J, Pardal G, Colegrove P. Wire+ arc additive manufacturing. Mater Sci Technol 2016;32:641–7.
[8] Sames WJ, List F, Pannala S, Dehoff RR, Babu SS. The metallurgy and processing science of metal additive manufacturing. Int Mater Rev 2016;61:315–60.
[9] Bermingham M, Nicastro L, Kent D, Chen Y, Dargusch M. Optimising the mechanical properties of ti-6Al-4V components produced by wire+ arc additive manufacturing with post-process heat treatments. J Alloys Compd 2018;753:247–55.
[10] Ding D, Pan Z, Cuiuri D, Li H. Wire-feed additive manufacturing of metal components: technologies, developments and future interests. Int J Adv Manuf Technol 2015;81:465–81.
[11] Martina F, Mehnen J, Williams SW, Colegrove P, Wang F. Investigation of the benefits of plasma deposition for the additive layer manufacture of Ti–6Al–4V. J Mater Process Technol 2012;212:1377–86.
[12] Drinkwater BW, Wilcox PD. In: Ultrasonic arrays for non-destructive evaluation: a review. 39. NDT & e International; 2006. p. 525–41.
[13] Bulavinov A, Pinchuk R, Pudovikov S, Boller C. Ultrasonic sampling phased array testing as a replacement for x-ray testing of weld joints in ship construction. Miscellaneous problems in maritime navigation, transport and shipping: marine navigation and safety of sea transportation91; 2011.
[14] Moles M, Dubé N, Labbé S, Ginzel E. Review of ultrasonic phased arrays for pressure vessel and pipeline weld inspections. 2005.
[15] Ramalho A, Santos TG, Bevans B, Smoqi Z, Rao P, Oliveira J. Effect of contaminations on the acoustic emissions during wire and arc additive manufacturing of 316L stainless steel. Addit Manuf 2022;51:102585.
[16] Hopkins D, Neau G, Le Ber L. Advanced phased-array technologies for ultrasonic inspection of complex composite parts. In: Proc., smart materials, structures, & NDT in aerospace; 2011.
[17] Taheri H, Hassen AA. Nondestructive ultrasonic inspection of composite materials: a comparative advantage of phased array ultrasonic. Appl Sci 2019;9:1628.
[18] Javadi Y, MacLeod CN, Pierce SG, Gachagan A. Ultrasonic phased array inspection of a Wire+ arc additive manufactured (WAAM) sample with intentionally embedded defects. Addit Manuf 2019;29:100806.
[19] Javadi Y, Sweeney NE, Mohseni E, MacLeod CN, Lines D, Vasilev M, Qiu Z, Mineo C, Pierce SG, Gachagan A. Investigating the effect of residual stress on hydrogen cracking in multi-pass robotic welding through process compatible non-destructive testing. J Manuf Process 2021;63:80–7.
[20] Lopez A, Bacelar R, Pires I, Santos TG, Sousa JP, Quintino L. Non-destructive testing application of radiography and ultrasound for wire and arc additive manufacturing. Addit Manuf 2018;21:298–306.
[21] Lopez AB, Santos J, Sousa JP, Santos TG, Quintino L. Phased array ultrasonic inspection of metal additive manufacturing parts. J Nondestruct Eval 2019;38:62.
[22] Chabot A, Laroche N, Carcreff E, Rauch M, Hascoët J-Y. Towards defect monitoring for metallic additive manufacturing components using phased array ultrasonic testing. J Intell Manuf 2019:1–11.
[23] Wu B, Pan Z, Ding D, Cuiuri D, Li H, Xu J, Norrish J. A review of the wire arc additive manufacturing of metals: properties, defects and quality improvement. J Manuf Process 2018;35:127–39.
[24] Knezovi N, Dolšak B. In-process non-destructive ultrasonic testing application during wire plus arc additive manufacturing. Adv Prod Eng Manag 2018;13:158–68.
[25] Reisgen U, Sharma R, Mann S, Oster L. Increasing the manufacturing efficiency of WAAM by advanced cooling strategies. Weld World 2020;64:1409–16.
[26] Vithanage RK, Mohseni E, Qiu Z, MacLeod C, Javadi Y, Sweeney N, et al. A phased array ultrasound roller probe for automated in-process/interpass inspection of multipass welds. IEEE Trans Ind Electron 2020;68(12):12781–90. https://doi.org/10.1109/TIE.2020.3042112.
[27] Bertocci F, Francalanci L, De Luca R, Bassani M, Gelli F, Palchetti P. Design of medical ultrasound probe: measurement system for the characterization of reverberations. In: 2018 IEEE international symposium medical measurements applications (MeMeA). IEEE; 2018. p. 1–6.
[28] Ho A, Zhao H, Fellowes JW, Martina F, Davis AE, Prangnell PB. On the origin of microstructural banding in Ti-6Al4V wire-arc based high deposition rate additive manufacturing. Acta Mater 2019;166:306–23.

[29] Jolly MR, Prabhakar A, Sturzu B, Hollstein K, Singh R, Thomas S, Foote P, Shaw A. Review of non-destructive testing (NDT) techniques and their applicability to thick walled composites. Procedia CIRP 2015;38:129–36.

[30] Zhang Y. Measuring acoustic attenuation of polymer materials using drop ball test. 2013.

[31] Olympus N. Ultrasonic transducers technical notes. In: Technical brochure: Olympus NDT, Waltham, MA. 2; 2006. p. 2.



https://dspace.org/

Development of a phased array ultrasound roller probe for inspection of wire + arc additive manufactured components

Vithanage, Randika K. W.; Mohseni, Ehsan; Lines, David; Loukas, Charalampos; Foster, Euan A. ...

2022-06-25
Elsevier
https://doi.org/10.1016/j.jmapro.2022.06.045
Vithanage RKW, Mohseni E, Lines D, et al., (2022) Development of a phased array ultrasound roller probe for inspection of wire + arc additive manufactured components, Journal of Manufacturing Processes, Volume 80, August 2022, pp. 765-774

Downloaded from a DSpace repository. https://dspace.org/